Solar Energy Materials & Solar Cells 286 (2025) 113595

Contents lists available at ScienceDirect

Solar Energy Materials and Solar Cells

journal homepage: www.elsevier.com/locate/solmat

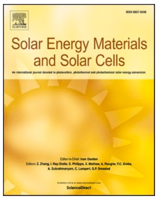

Optimized optical and electrical properties for silicon heterojunction solar cells with an indium tin oxide buffer layer

Daxue Du [a,b], Jianjun Liang [a,b,*], Wenzhong Shen [c,**]

[a] Shanghai Hency Solar Technology Co., Ltd, Shanghai, 201109, PR China
[b] Shanghai Electric Group Hency Solar Technology (Nantong) Co., Ltd, Nantong, 226100, PR China
[c] Institute of Solar Energy, School of Physics and Astronomy, Shanghai Jiao Tong University, Shanghai, 200240, PR China

ARTICLE INFO

Keywords:
Indium tin oxide (ITO)
Silicon heterojunction solar cell
Buffer layer
Complex refractive index
Resistivity

ABSTRACT

Indium tin oxide (ITO) layers prepared with high power have significantly contributed to enhancing the crystal quality of films and the performance of silicon heterojunction solar cells. However, this process typically results in sputtering damage, which degrades photovoltaic efficiency. We have designed a thin ITO buffer layer prepared at low power and O_2 concentration, followed by an outer ITO layer prepared at high power and high O_2 concentration. Thus, the bilayer ITO film demonstrates superior optical and electrical properties, attributed to the optimized complex refractive index and resistivity achieved through synergistic control of power and oxygen levels, compared to monolayer ITO films. The leakage risk from the addition of an interface was suppress without compromising the open-circuit voltage. Consequently, the average efficiency improves to 25.36 % with a gain of 0.11 %, benefiting from optimized short-circuit current density and fill factor.

1. Introduction

The N-type silicon heterojunction (SHJ) solar cell stands out as a leading candidate for industrial-scale applications due to its excellent passivation qualities, streamlined fabrication process, and minimal degradation [1–3]. Furthermore, SHJ technology has recently achieved the highest certified efficiency among all silicon-based photovoltaic devices [4,5]. In standard configurations, transparent conductive oxide (TCO) layers are applied on silicon substrates to enable the transfer of carriers to metal fingers, addressing the limited lateral conductivity of microcrystalline silicon [6–8]. Additionally, TCO also serves to reduce reflection and protect the substrate [9,10]. Among the diverse TCO materials [7,11–15], indium tin oxide (ITO) dominates mass production because of its excellent optical transmittance (near 90 % in the visible region), low resistivity (10^{-4} Ω cm), and exceptional corrosion resistance to acetic acid [16–18].

Increasing the sputtering power during ITO deposition typically lowers resistivity and supports high production throughput [19], while a high power causes sputtering damage to the microcrystalline silicon layers below the ITO and elevated parasitic absorption in the ITO films [20,21]. Mengxiao Wang et al. [21] reported that improvements in ITO films cause device gains in short-circuit current density (J_{SC}) and fill factor (FF) as the sputtering power increased from 1 kW to 5 kW, thus obtaining an optimal power conversion efficiency (PCE) of 25.22 % for SHJ solar cells. However, PCE is slightly decreased with an higher sputtering power. Encouragingly, many studies have demonstrated that adjusting the oxygen content during ITO deposition effectively controls the complex refractive index, carrier mobility, and resistivity [22–25]. Therefore, introducing a low-power-deposited ITO buffer layer atop the microcrystalline silicon offers a feasible multilayered solution, which has proven effective in functional layers of SHJ solar cells [26–30].

In this work, ITO buffer layer- was introduced to obtain more excellent optical and electrical properties through power and oxygen concentration optimization. With the application of an ITO buffer layer, carrier concentration and mobility were simultaneously enhanced due to a reduction in chemisorbed oxygen and a rise in oxygen vacancies, thereby achieving lower resistivity. Consequently, both optical and electrical properties were optimized, as indicated by the improved - J_{SC} and FF. Additionally, the open-circuit voltage (V_{OC}) of SHJ solar cells with bilayer ITO films experienced a minor reduction due to leakage at the newly introduced interface, which was mitigated through O_2 modulation. Our findings offer valuable insights for the development of high-efficiency and high-yield SHJ solar cells.

---

* Corresponding author. Shanghai Hency Solar Technology Co., Ltd, Shanghai, 201109, PR China.
** Corresponding author.
E-mail addresses: liangjj@shanghai-electric.com (J. Liang), wzshen@sjtu.edu.cn (W. Shen).

https://doi.org/10.1016/j.solmat.2025.113595
Received 23 December 2024; Received in revised form 12 February 2025; Accepted 17 March 2025

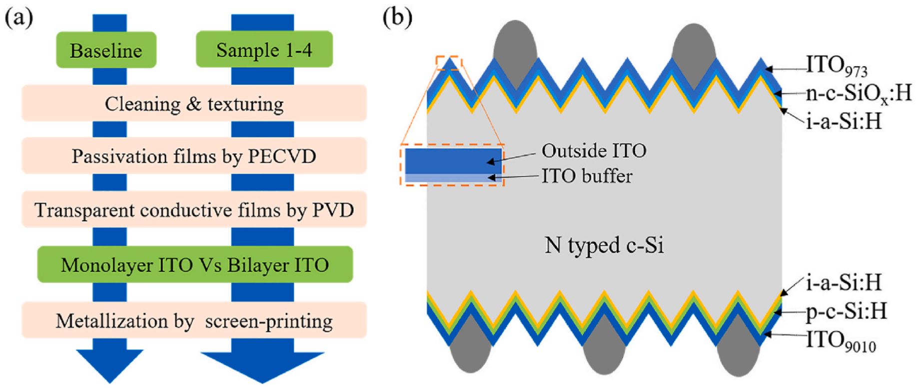

Fig. 1. (a) The fabricated process for SHJ solar cell. (b) Schematic structure of the SHJ solar cell.

Table 1
Fabrication parameters of the front ITO films including deposition power, time and O_2 content.

Sample	ITO buffer			outside ITO		
	Power (kW)	Time (s)	O_2 content (%)	Power (kW)	Time (s)	O_2 content (%)
BL	–	–	–	12	96	2.40
S1	9	24	2.40	13	72	2.40
S2	9	24	2.20	13	72	2.47
S3	9	24	2.00	13	72	2.53
S4	9	24	1.80	13	72	2.60

2. Experiments and methods

2.1. Device fabrication

To fabricate the SHJ device, a 120 μm thick n-type monocrystalline silicon wafer (182 mm × 105 mm) was chosen as the substrate. As depicted in Fig. 1(a), the silicon wafer undergoes sequential texturing using KOH solutions, followed by the deposition of hydrogenated amorphous and microcrystalline silicon passivation films via plasma enhanced chemical vapor deposition (PECVD). Subsequently, the back ITO ($In_2O_3/SnO_2 = 90/10$) film is deposited using the physical vapor deposition (PVD) technique. The front thin ITO ($In_2O_3/SnO_2 = 97/3$) buffer layer was prepared with a lower power, and then the ITO layer was prepared with a higher power. Finally, silver grids were fabricated using screen-printing and subsequently annealed at 200 °C [31]. Fig. 1 (b) presents the schematic structure of the SHJ solar cell, which includes an ITO buffer layer.

Table 1 lists the process parameters for the front ITO films without and with a buffer layer. To minimize sputtering damage, the buffer layer was deposited at a lower power of 9 kW for 24 s, while a higher power of 13 kW for 72 s was employed for the outer ITO layer to maintain consistent thickness. In addition, the O_2 concentration was modulated to further optimize the optical and electric properties of bilayer ITO films.

2.2. Characterization

The surface morphology and grain sizes of ITO films were observed by field-emission Scanning electron microscope (SEM, Zeiss Ultra Plus, Germany). The ITO films were characterized by X-ray diffraction (XRD, D8 ADVANCE Da Vinci, Bruker). The elemental contents of ITO films were measured using an X-ray photoecectron spectroscopy (XPS, S8 Tiger II, Germany). The thickness and complex refractive indexes of the ITO films were analyzed by an optical ellipsometer (Raditech SE-950). The electrical parameters of the ITO films, such as carrier mobility, carrier concentration, and resistivity, were monitored by a Hall tester

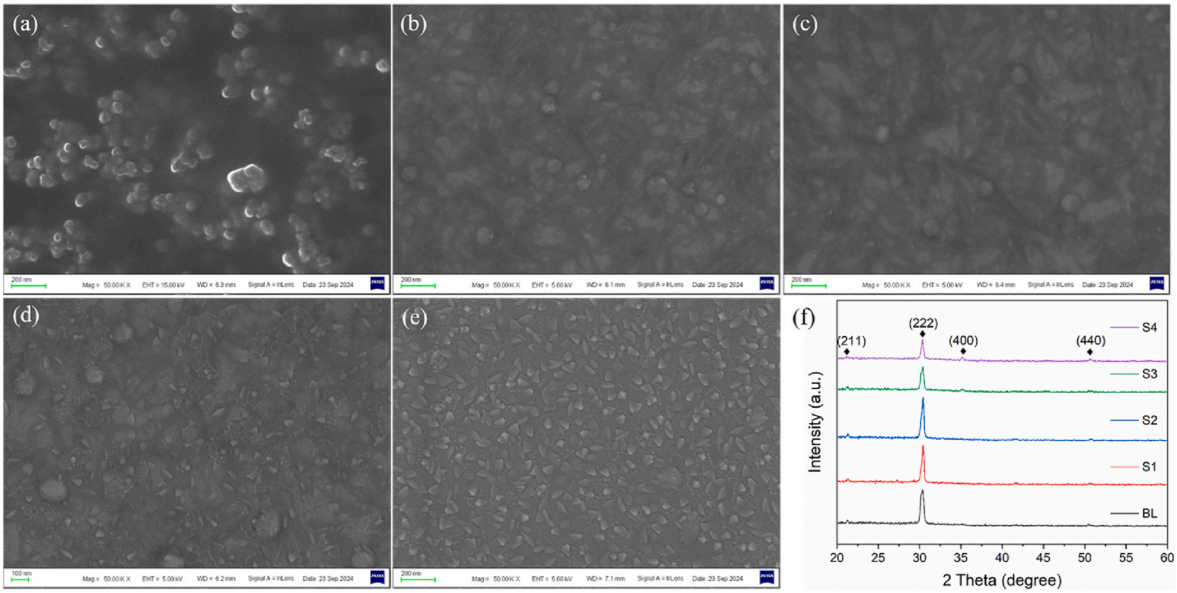

Fig. 2. SEM images of different front ITO films without and with a buffer layer, (a) BL, (b) S1, (c) S2, (d) S3, (e) S4. (f) XRD spectra of different front ITO films without and with a buffer layer.

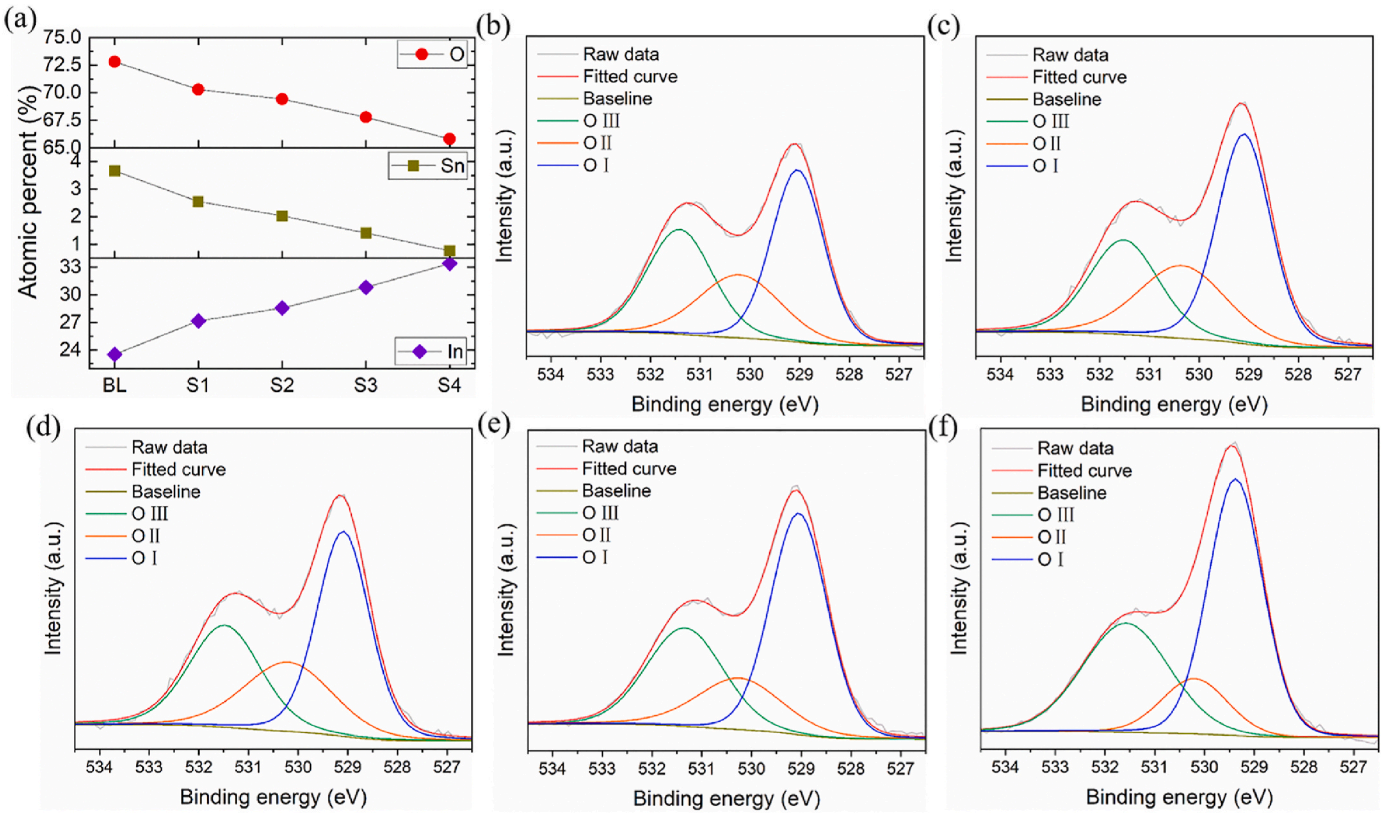

Fig. 3. (a) Atomic percent in front ITO films extracted from XPS spectra. O 1s spectra of front ITO films without and with a buffer layer, (b) BL, (c) S1, (d) S2, (e) S3, (f) S4.

Table 2
Atomic percent of In, Sn and O in front ITO films.

Atomic	BL (%)	S1 (%)	S2 (%)	S3 (%)	S4 (%)
In	23.52	27.17	28.56	30.81	33.42
Sn	3.67	2.55	2.03	1.41	0.77
O	72.81	70.28	69.41	67.78	65.81

(Swin HALL8800-II). The square resistance of the substrate was measured using a double electrodynamic four-probe tester (RTS-5, China). The Quantum Efficiency Measurements system (PVE300-IVT210, Bentham) collected EQE and transmission spectra in the wavelength range from 300 to 1180 nm. Finally, Vision VS-6831S (AAA level) tested the I-V parameters in air under standard simulated AM 1.5G sunlight irradiance.

3. Results and discussion

The SEM images of different ITO films deposited on glasses are shown in Fig. 2(a–e). Clusters of nanoparticles approximately 50 nm in size are visible on the surface of the monolayer ITO (baseline, BL), resulting in significant surface roughness. In contrast, bilayer ITO films (S1-S4) exhibit smoother surfaces, attributed to the low-power preparation of the buffer layer. Owing to the improvement in O_2 concentration supply from 2.40 % to 2.60 %, the ITO grains grow bigger and denser. As presented in 2(f), the XRD spectra reveal diffraction peaks of ITO at 30.4° corresponding to the (222) crystal planes (JCDS#No.6-0416), which is the dominant characteristic peak in all films [24,32]. As the O_2 concentration increases, the intensity of the (222) diffraction peak initially rises, reaching a maximum at S2, and subsequently declines. A notable observation is that the attenuation of the (222) peak occurs simultaneously with the development of the (400) diffraction

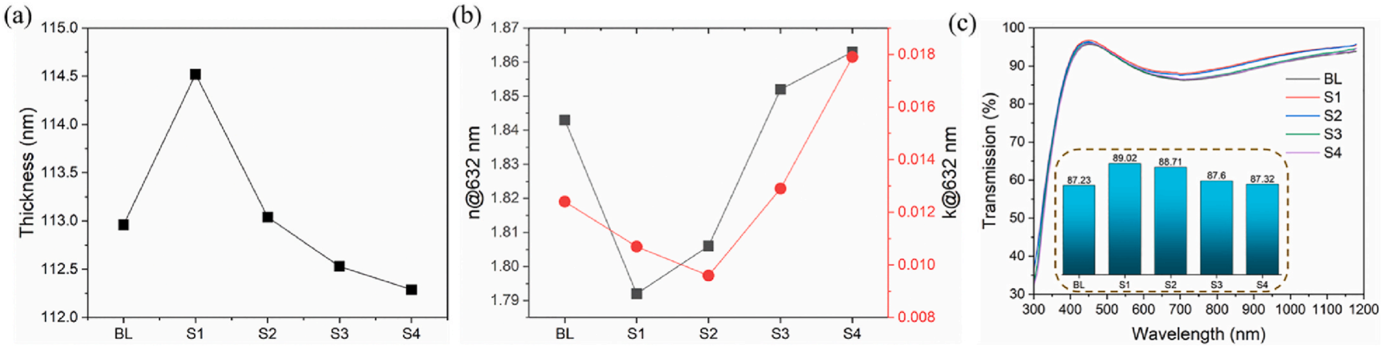

Fig. 4. Optical characteristics of the front ITO films without and with a buffer layer: (a) thickness, (b) refractive index, n (left) and extinction coefficient, k (right), and (c) transmission.

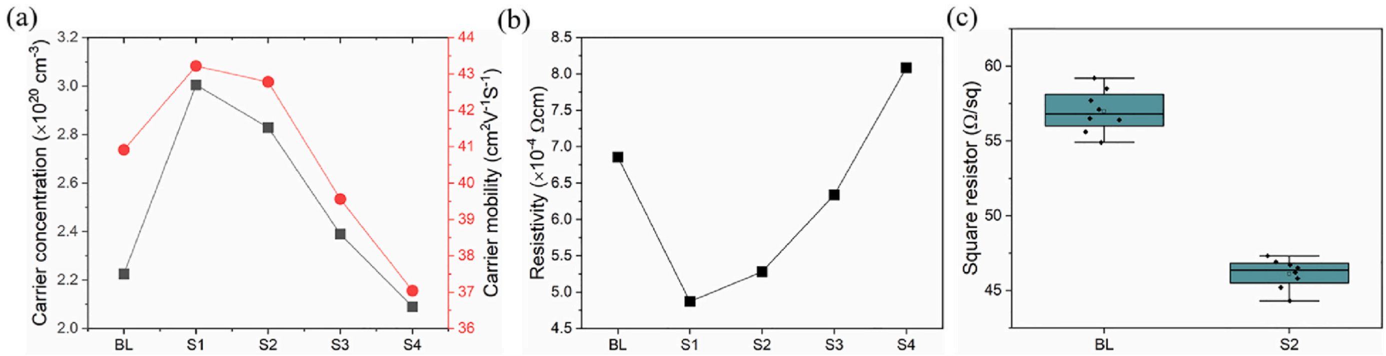

Fig. 5. Electrical characteristics of the front ITO films without and with a buffer layer: (a) carrier concentration (left) and carrier mobility (right), and (b) resistivity. (c) Statistical square resistances of BL and S2.

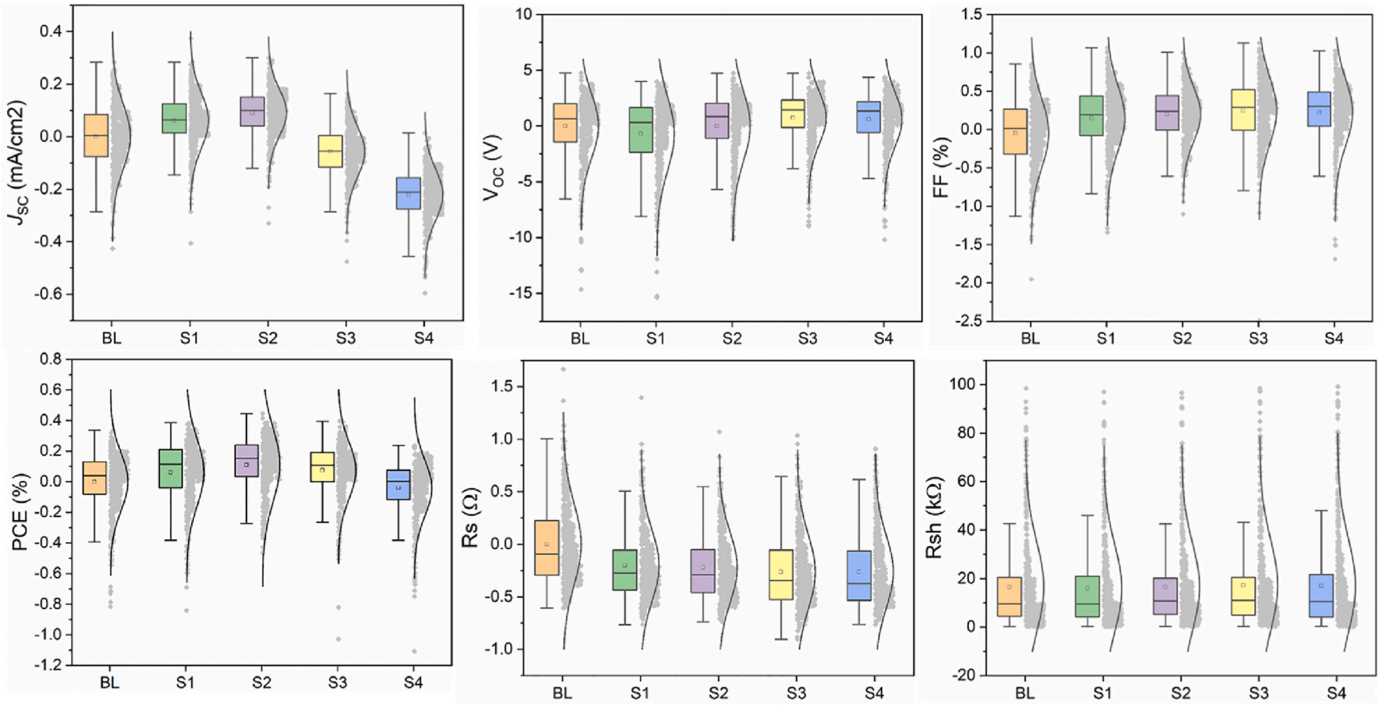

Fig. 6. Normalized photovoltaic parameters of the SHJ solar cells without and with ITO buffer layer, including J_{SC}, V_{OC}, FF, PCE, R_S and R_{Sh}.

Table 3

Photovoltaic performance of SHJ solar cell without and with ITO buffer layer.

Samples	J_{SC} (mA/cm^2)	V_{OC} (mV)	FF (%)	PCE (%)	R_s (mΩ)	R_{sh} (kΩ)
BL	0	0	0	0	0	0
S1	+0.06	−0.70	+0.15	+0.06	−0.20	−0.55
S2	+0.09	−0.01	+0.20	+0.11	−0.22	−0.09
S3	−0.06	+0.73	+0.24	+0.05	−0.26	+0.71
S4	−0.22	+0.59	+0.23	−0.07	−0.26	+0.51

peak.

Fig. 3(a) illustrates that incorporating the ITO buffer layer leads to a decrease in the atomic percentages of O and Sn, as detailed in Table 2. Interestingly, an increase in O_2 concentration from 2.40 % to 2.60 % in the outer ITO films is accompanied by a downward trend in O atomic percentage, decreasing from 70.28 % to 65.81 %. Elevating both the power and O_2 concentration increases the In_2O_3 content while decreasing the SnO_2 content, effectively reducing the Sn^{4+} doping level in the ITO films. As shown in Fig. 3(b–f), the O 1s spectra comprise three distinct components: O I, O II, and O III, corresponding to binding energies of 531.6 eV, 530.4 eV, and 529.1 eV, respectively [14,33]. The peak at 531.6 eV, representing the highest binding energy, is attributed to absorbed hydroxyl groups, while the 529.1 eV peak corresponds to lattice oxygen in crystalline ITO, and the 530.4 eV peak is associated with oxygen vacancies. A higher O II intensity in S1 relative to BL implies the presence of numerous oxygen vacancies, which enhance free carrier generation. Concurrently, a reduction in O III intensity reflects a decrease in chemisorbed oxygen, leading to enhanced carrier mobility [34].

Fig. 4(a) exhibits that the thickness difference between the bilayer and monolayer ITO is kept within 1.7 nm by employing a layered power and O_2 modulation strategy. As shown in Fig. 4(b), the refractive index (n) and extinction coefficient (k) of ITO films at 632 nm are displayed. The optical properties of ITO are significantly improved by obtaining lower n and k due to the introduction of a buffer layer. However, the n and k of the bilayer ITO gradually increased after elevating the O_2 concentration, achieving the minimum n at S1 and the minimum k at S2, respectively. Fig. 4(c) displays the transmission of the ITO films across the wavelength range of 300 nm–1180 nm. The transmittance of five

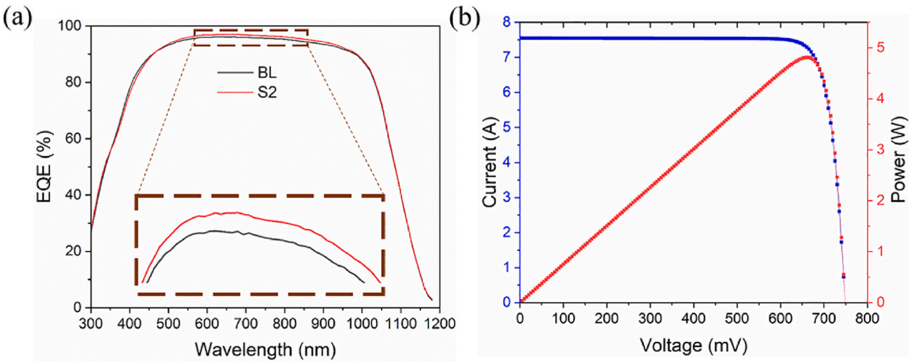

Fig. 7. (a) EQE curves of the SHJ solar cell without and with ITO buffer layer. (b) the representative the I-V and P-V curves of SHJ solar cell at S2 with ITO buffer layer.

different ITO films remained basically consistent in the wavelength 300 nm–400 nm, evidencing the similar bandgap (~3.7 eV), as determined by the Tauc plotting method [35,36]. Above 500 nm, S1 and S2 demonstrate much higher transmission than the other three samples due to the combined effect of smaller n and k [37,38], where a smaller n reduces reflection loss at the interface between air and nc-SiOx:H ($\sqrt{n_{\mathrm{air}} n_{\mathrm{nc-SiOx:H}}} \approx 1.7$ [39]), and a smaller k minimizes parasitic absorption. The inset shows that S1 obtained the maximum transmittance of 89.02 %, followed by 88.71 % of S2 and 87.60 % of S3.

As displayed in Fig. 5(a), The carrier concentration (N) of front ITO films was significantly improved from 2.23×10^{20} cm^{-3} to 3.01×10^{20} cm^{-3} by introducing a buffer layer. Nevertheless, N of the bilayer ITO film gradually reduces to 2.09×10^{20} cm^{-3} with increasing O_2 concentration. The decrease in N with increasing O_2 concentration is attributed to reduced oxygen vacancies and Sn doping concentration, consistent with the results shown in Fig. 3(b–c). Carrier mobility (μ) exhibits a similar trend compared to N in Fig. 5(b), achieving the largest values of 43.2 $\mathrm{cm}^2/\mathrm{V{\cdot}S}$ at S1. Decay of μ in the ITO with increasing O_2 concentration can be traced back to an improvement in chemisorbed oxygen [40], which is consistent with the change in O III intensity in Fig. 3(b–f). With the increase in chemisorbed oxygen, carrier scattering is enhanced, resulting in a reduction of μ. The resistivity (ρ) is inversely proportional to the product of N and μ according to Equation (1) [20],

$$\rho = 1/N\mu e \tag{1}$$

where e is electron charge. Consequently, ρ of the ITO films decreases from 6.86×10^{-4} $\Omega{\cdot}\mathrm{cm}$ to 4.87×10^{-4} $\Omega{\cdot}\mathrm{cm}$ before increasing to 8.08×10^{-4} Ω cm. The BL possess an average square resistance of 56.9 Ω/sq, as shown in Fig. 5(c). By introducing ITO buffer layer and regulating O_2 concentration, the square resistance decreases notably to 46.1 Ω/sq at S2.

The bilayer ITO was specifically designed to achieve improved electrical performance in the thin buffer layer prepared at low power and O_2 concentration, while also enhancing optical performance in the thicker outer layer prepared at higher power and O2 concentration. Consequently, the bilayer ITO demonstrates superior combined optical and electrical performance compared to the monolayer ITO.

The optical and electrical properties of the SHJ solar cell are influenced by the ITO buffer layer and the subsequent O_2 treatment. Hence, we depicted the normalized statistical J–V parameters on 4 different bilayer front ITO arrangements in Fig. 6 with the monolayer front ITO as a baseline. And the parameters are summarized in Table 3. S1 presents a 0.02 $\mathrm{mA/cm}^2$ improvement in average J_{SC} compared to BL while S2 provide a 0.08 $\mathrm{mA/cm}^2$ gain, which is a slight difference from Fig. 4(c), indicating that the optimized properties of the films cannot fully migrate to the photovoltaic devices. Continuing to improve the O_2 concentration, the average J_{SC} produces a severe drop in S3 and S4.

Nevertheless, the V_{OC} was observed to be reduced by about 0.7 mV in S1 than BL with ITO buffer layer deposited with a power of 9 kW, which originated from a smaller shunt resistance (R_{sh}). Adding an interface tends to cause leakage manifested by a decrease in R_{sh} [41], which is well ameliorated by increasing the O_2 concentration, and thus V_{OC} gets boosted from S1 to S4. Meanwhile, the FF of all SHJ solar cells with the ITO buffer layer increased by approximately 0.2 %, corresponding to the reduction in series resistance (Rs). Compared to monolayer ITO, the Rs of bilayer ITO improve by 0.20 mΩ for S1, 0.22 mΩ for S2, 0.26 mΩ for S3, and 0.26 mΩ for S4, respectively, brought by reduced sputtering damage for microcrystalline silicon films and reduced square resistance for ITO films. Based on the results of J_{SC}, V_{OC} and FF, the average PCE of SHJ solar cells can also be obtained using bilayer ITO films. Therefore, 0.11 % of the maximum efficiency gain was achieved at S2.

Fig. 7(a) offers the external quantum efficiencies (EQE) of the SHJ solar cell with monolayer (BL) and bilayer (S2) ITO films. The EQE values get slightly improvement during the wavelength of 500 nm–1000 nm with introducing ITO buffer layer, as seen in the local zoomed-in view. As shown in Fig. 7(b), the representative the I-V and P-V curves of the large-size SHJ solar cell (191.1 cm^2) with ITO buffer layer were provided, achieving the average PCE of 25.36 % and power of 4.85 W.

4. Conclusions

In summary, we investigated the optical and electrical performance of four bilayer front ITO structures on industrial SHJ solar cells, using the monolayer ITO film as a baseline. The bilayer ITO films were fabricated with high power and high O_2 concentration to reduce the refractive index and extinction coefficient, leading to enhanced optical properties. Specifically, the refractive index decreased from 1.84 to 1.80, and the extinction coefficient reduced from 0.012 to 0.009, resulting in a 0.3 % increase in J_{SC}. Furthermore, the resistivity of ITO films was reduced from 6.86×10^{-4} $\Omega{\cdot}\mathrm{cm}$ to 4.87×10^{-4} $\Omega{\cdot}\mathrm{cm}$ due to the introduction of an ITO buffer layer, yielding a 0.2 % improvement in FF. As a result, we achieved an average-PCE of 25.36 % for industrial SHJ solar cells with bilayer front ITO films, marking an over 0.1 % improvement compared to devices without the ITO buffer layer.

CRediT authorship contribution statement

Daxue Du: Writing – original draft, Methodology, Investigation, Formal analysis, Data curation, Conceptualization. **Jianjun Liang:** Resources, Project administration, Methodology, Conceptualization. **Wenzhong Shen:** Writing – review & editing, Funding acquisition, Formal analysis.

Declaration of competing interest

The authors declare that they have no known competing financial interests or personal relationships that could have appeared to influence the work reported in this paper.

Acknowledgments

This work Supported by the Major State Basic Research Development Program of China (Grant No. 2022YFB4200101) and Inner Mongolia Science and Technology Project (Grant No. 2022JBGS0036).

Data availability

Data will be made available on request.

References

[1] C. Ballif, F.-J. Haug, M. Boccard, P.J. Verlinden, G. Hahn, Status and perspectives of crystalline silicon photovoltaics in research and industry, Nat. Rev. Mater. 7 (2022) 597–616.

[2] W. Shen, Y. Zhao, F. Liu, Highlights of mainstream solar cell efficiencies in 2023, Front. Energy 18 (2024) 8–15.

[3] B. Vicari Stefani, M. Kim, Y. Zhang, B. Hallam, M.A. Green, R.S. Bonilla, C. Fell, G. J. Wilson, M. Wright, Historical market projections and the future of silicon solar cells, Joule 7 (2023) 2684–2699.

[4] H. Lin, M. Yang, X. Ru, G. Wang, S. Yin, F. Peng, C. Hong, M. Qu, J. Lu, L. Fang, C. Han, P. Procel, O. Isabella, P. Gao, Z. Li, X. Xu, Silicon heterojunction solar cells with up to 26.81% efficiency achieved by electrically optimized nanocrystalline-silicon hole contact layers, Nat. Energy 8 (2023) 789–799.

[5] H. Wu, F. Ye, M. Yang, F. Luo, X. Tang, Q. Tang, H. Qiu, Z. Huang, G. Wang, Z. Sun, H. Lin, J. Wei, Y. Li, X. Tian, J. Zhang, L. Xie, X. Deng, T. Yuan, M. Yu, Y. Liu, P. Li, H. Chen, S. Zhou, Q. Xu, P. Li, J. Duan, J. Chen, C. Li, S. Yin, B. Liu, C. Sun, Q. Su, Y. Wang, H. Deng, T. Xie, P. Gao, Q. Kang, Y. Zhang, H. Yan, N. Yuan, F. Peng, Y. Yuan, X. Ru, B. He, L. Chen, J. Wang, J. Lu, M. Qu, C. Xue, J. Ding, L. Fang, Z. Li, X. Xu, Silicon heterojunction back-contact solar cells by laser patterning, Nature 635 (2024) 604–609.

[6] Z. Sun, X. Chen, Y. He, J. Li, J. Wang, H. Yan, Y. Zhang, Toward efficiency limits of crystalline silicon solar cells: recent progress in high-efficiency silicon heterojunction solar cells, Adv. Energy Mater. 12 (2022) 2200015.

[7] G. Dong, J. Sang, C.-W. Peng, F. Liu, Y. Zhou, C. Yu, Power conversion efficiency of 25.26% for silicon heterojunction solar cell with transition metal element doped indium oxide transparent conductive film as front electrode, Prog. Photovolt. 30 (2022) 1136–1143.

[8] S. Mandal, S. Mitra, S. Dhar, H. Ghosh, C. Banerjee, S.K. Datta, H. Saha, Potential of ITO nanoparticles formed by hydrogen treatment in PECVD for improved performance of back grid contact crystalline silicon solar cell, Appl. Surf. Sci. 349 (2015) 116–122.

[9] F. Meyer, A. Savoy, J.J.D. Leon, M. Persoz, X. Niquille, C. Alleb’e, S. Nicolay, H. Franz-Josef, A. Ingenito, C. Ballif, Optimization of front SiNx/ITO stacks for high-efficiency two-side contacted c-Si solar cells with co-annealed front and rear, Sol. Energy Mater. Sol. Cells 219 (2021) 110815.

[10] H.W. Du, J. Yang, M. Gao, Y. Li, Y.Z. Wan, F. Xu, Z.Q. Ma, The bifunctional tin-doped indium oxide as hole-selective contact and collector in silicon heterojunction solar cell with a stable intermediate oxide layer, Sol. Energy 155 (2017) 963–970.

[11] S. Li, Z. Shi, Z. Tang, X. Li, Comparison of ITO, In2O3:Zn and In2O3:H transparent conductive oxides as front electrodes for silicon heterojunction solar cell applications, Vacuum 145 (2017) 262e267.

[12] A. Cruza, E.-C. Wanga, A.B. Morales-Vilchesa, D. Mezab, S. Neuberta, B. Szyszkac, R. Schlatmanna, B. Stannowski, Effect of front TCO on the performance of rear-junction silicon heterojunction solar cells: insights from simulations and experiments, Sol. Energy Mater. Sol. Cells 195 (2019) 339–345.

[13] A. Cruz, F. Ruske, A. Eljarrat, P.P. Michalowski, A.B. Morales-Vilches, S. Neubert, R. Schlatmann, E.-C. Wang, C.T. Koch, B. Szyszka, B. Stannowski, Influence of silicon layers on the growth of ITO and AZO in silicon heterojunction solar cell, IEEE J. Photovolt. 10 (2020) 703.

[14] C. Han, L. Mazzarella, Y. Zhao, G. Yang, P. Procel, M. Tijssen, A. Montes, L. Spitaleri, A. Gulino, X. Zhang, O. Isabella, M. Zeman, High-mobility hydrogenated fluorine-doped indium oxide film for passivating contacts c-Si solar cells, ACS Appl. Mater. Interfaces 11 (2019) 45586–45595.

[15] C. Han, Y. Zhao, L. Mazzarella, R. Santbergen, A. Montes, P. Procel, G. Yang, X. Zhang, M. Zeman, O. Isabella, Room-temperature sputtered tungsten-doped indium oxide for improved current in silicon heterojunction solar cells, Sol. Energy Mater. Sol. Cells 227 (2021) 111082.

[16] R. Saive, M. Boccard, T. Saenz, S. Yalamanchili, C.R. Bukowsky, P. Jahelka, Z.J. Yu, J. Shi, Z. Holmanb, H.A. Atwater, Silicon heterojunction solar cells with effectively transparent front contacts, Sustain. Energy Fuels 1 (2017) 593.

[17] A.H.T. Le, S. Ahn, S. Han, J. Kim, S.Q. Hussain, H. Park, C. Park, C.P.T. Nguyen, V. A. Dao, J. Yi, Effective optimization of indium tin oxide films by a statistical approach for shallow emitter based crystalline silicon solar cell applications, Sol. Energy Mater. Sol. Cells 125 (2014) 176–183.

[18] X. Li, X. Jia, L. Zhao, X. Xu, L. Wen, S. Qu, C. Peng, K. Xin, J. Xiao, S. Zhou, L. Zhang, Y. Zuo, W. Wang, Corrosion resistance improvement of transparent conductive oxide films to the acidic etching during the electroplating preparation of copper electrodes on silicon heterojunction solar cells, Sol. Energy Mater. Sol. Cells 282 (2025) 113360.

[19] G.T. Chavan, E.-C. Cho, Y. Kim, M.Q. Khokhar, S.Q. Hussain, J. Yi, Z. Ahmad, P. Rosaiah, C.-W. Jeon, A brief review of transparent conducting oxides (TCO): the influence of different deposition techniques on the efficiency of solar cells, Nanomaterials 13 (2023) 1226.

[20] A.H.T. Lea, V.A. Dao, D.P. Phamd, S. Kime, S. Duttad, C.P.T. Nguyend, Y. Leee, Y. Kimd, J. Yi, Damage to passivation contact in silicon heterojunction solar cells by ITO sputtering under various plasma excitation modes, Sol. Energy Mater. Sol. Cells 192 (2019) 36–43.

[21] B. Demaurex, S.D. Wolf, A. Descoeudres, Z.C. Holman, C. Ballif, Damage at hydrogenated amorphous/crystalline silicon interfaces by indium tin oxide overlayer sputtering, Appl. Phys. Lett. 101 (2012) 171604.

[22] S. Kirner, M. Hartig, L. Mazzarella, L. Korte, T. Frijnts, H. Scherg-Kurmes, S. Ring, B. Stannowski, B. Rech, R. Schlatmann, The influence of ITO dopant density on J-V characteristics of silicon heterojunction solar cells: experiments and simulations, Energy Proc. 77 (2015) 725–732.

[23] D. Qiu, W. Duan, A. Lambertz, K. Bittkau, K. Qiu, U. Rau, K. Ding, Effect of oxygen and hydrogen flow ratio on indium tin oxide films in rear-junction silicon heterojunction solar cells, Sol. Energy 231 (2022) 578–585.

[24] W. Gong, G. Wang, Y. Gong, L. Zhao, L. Mo, H. Diao, H. Tian, W. Wang, J. Zong, W. Wang, Investigation of In2O3:SnO2 films with different doping ratio and application as transparent conducting electrode in silicon heterojunction solar cell, Sol. Energy Mater. Sol. Cells 234 (2022) 111404.

[25] S.Y. Herasimenka, W.J. Dauksher, M. Boccard, S. Bowden, ITO/SiOx:H stacks for silicon heterojunction solar cells, Sol. Energy Mater. Sol. Cells 158 (2016) 98–101.

[26] L. Wen, L. Zhao, G. Wang, X. Jia, X. Xu, S. Qu, X. Li, X. Zhang, K. Xin, J. Xiao, X. Zhang, S. Zhou, Y. Zuo, W. Wang, Boron-doped amorphous buffer layer for p-type microcrystalline silicon emitter to prepare efficient silicon heterojunction solar ce, Sol. Energy Mater. Sol. Cells 278 (2024) 113216.

[27] C. Peng, C. He, H. Wu, S. Huang, C. Yu, X. Su, S. Zou, Improving the performance of high-efficiency silicon heterojunction solar cells through low-temperature deposition of an i-a-Si:H anti-epitaxial buffer layer, Sol. Energy Mater. Sol. Cells 273 (2024) 112952.

[28] X. Ru, M. Qu, J. Wang, T. Ruan, M. Yang, F. Peng, W. Long, K. Zheng, H. Yan, X. Xu, 25.11% efficiency silicon heterojunction solar cell with low deposition rate intrinsic amorphous silicon buffer layers, Sol. Energy Mater. Sol. Cells 215 (2020) 110643.

[29] Q. Tang, W. Duan, A. Lambertz, K. Bittkau, M.A. Yaqin, Y. Zhao, K. Zhang, Q. Yang, D. Qiu, F. Gunkel, M. Weber, U. Rau, K. Ding, 85% indium reduction for high-efficiency silicon heterojunction solar cells with aluminum-doped zinc oxide contacts, Sol. Energy Mater. Sol. Cells 251 (2023) 112120.

[30] L. Barraud, Z.C. Holman, N. Badel, P. Reiss, A. Descoeudres, C. Battaglia, S.D. Wolf, C. Ballif, Hydrogen-doped indium oxide/indium tin oxide bilayers for high-efficiency silicon heterojunction solar cells, Sol. Energy Mater. Sol. Cells 15 (2013) 151–156.

[31] D. Du, H. Huang, X. Li, S. Ma, D. Zhao, R. Li, H. Huang, Z. Hao, F. Meng, L. Li, L. He, D. Ding, Z. Liu, W. Zhang, W. Shen, Low-cost metallization based on Ag/Cu fingers for exceeding 25% efficiency in industrial silicon heterojunction solar cells, Sol. RRL 8 (2024) 2400052.

[32] A. Valla, P. Carroy, F. Ozanne, D. Muñoz, Understanding the role of mobility of ITO films for silicon heterojunction solar cell applications, Sol. Energy Mater. Sol. Cells 157 (2016) 874–880.

[33] M. Wang, G. Wang, W. Gong, S. Cheng, L. Zhao, X. Xu, D. Gong, F. Ye, L. Mo, H. Diao, W. Wang, Influence of In2O3:SnO2 films at different sputtering power on efficiency and stability of heterojunction solar cells, Sol. Energy Mater. Sol. Cells 253 (2023) 112229.

[34] H.I. Yeom, J.B. Ko, G. Mun, S.H.K. Park, High mobility polycrystalline indium oxide thin-film transistors by means of plasma-enhanced atomic layer deposition, J. Mater. Chem. C 4 (2016) 6873–6880.

[35] M. Ahmed, A. Bakry, A. Qasem, H. Dalir, The main role of thermal annealing in controlling the structural and optical properties of ITO thin film layer, Opt. Mater. 113 (2021) 110866.

[36] D. Du, D. Zhang, H. Liu, W. Shen, Enhanced carrier transport and optical gains in perovskite solar cells based on low-temperature prepared TiO2@SnO2 nanocrystals, J. Alloys Compd. 983 (2024) 173714.

[37] Z. Gao, G. Lin, Y. Chen, Y. Zheng, N. Sang, Y. Li, L. Chen, M. Li, Moth-eye nanostructure PDMS films for reducing reflection and retaining flexibility in ultra-thin c-Si solar cells, Sol. Energy 205 (2020) 275–281.

[38] D. Du, Z. Xu, L. Wang, Y. Guo, S. Liu, T. Yu, C. Wang, F. Wang, H. Wang, The broadband and omnidirectional antireflective performance of perovskite solar cells with curved nanostructures, Sol. Energy 224 (2021) 10–17.

[39] D. Qiu, A. Lambertz, W. Duan, L. Mazzarella, P. Wagner, A. Morales-Vilches, G. Yang, P. Procel, O. Isabella, B. Stannowski, K. Ding, A review: application of doped hydrogenated nanocrystalline silicon oxide in high efficiency solar cell devices, Adv. Sci. 11 (2024) 2403728.

[40] Y. Ren, P. Liu, R. Liu, Y. Wang, Y. Wei, L. Jin, G. Zhao, The key of ITO films with high transparency and conductivity: grain size and surface chemical composition, J. Alloys Compd. 893 (2022) 162304.

[41] K.-H. Choi, J. Kim, Y.-J. Noh, S.-I. Na, H.-K. Kim, Ag nanowire-embedded ITO films as a near-infrared transparent and flexible anode for flexible organic solar cells, Sol. Energy Mater. Sol. Cells 110 (2013) 147–153.